sensors

MDPI

Article

Adaptive Dual-Beam Tracking for IRS-Assisted High-Speed Multi-UAV Communication Networks

Zhongquan Peng [1,2], Guanglong Huang [3,*], Qian Deng [4] and Xiaopeng Liang [4]

[1] School of Intelligent Manufacturing, Jiangxi Institute of Applied Science and Technology, Nanchang 330100, China; zhongquanpeng@163.com
[2] College of Electronics and Information, Hangzhou Dianzi University, Hangzhou 310018, China
[3] Haikou Bureau of Science, Technology, Industry and Informatization, Haikou 570100, China
[4] School of Information and Communication Engineering, Hainan University, Haikou 570228, China; dqian108@163.com (Q.D.); liangxiaopeng@hainan.edu.cn (X.L.)
* Correspondence: huanggl8998@126.com

Abstract

This study investigates the communication network (MUAVN) of intelligent reflecting surface (IRS)-assisted high-speed multiple unmanned aerial vehicles, considering that highly dynamic UAVs may incur poor performance due to severe channel fading and rapid channel changes. Our objective is to design an adaptive dual-beam tracking scheme that mitigates beam misalignment, enhances the performance of the worst-case UAV, and sustains reliable communication links in the high-speed MUAVNs (HSMUAVNs). We first exploit an attention-based double-layer long short-term memory network to predict the spatial angle information of each UAV, which yields optimal beam coverage that matches to the UAV's actual flight trajectory. Then, a worst-case UAV's received beam components signal-to-interference plus noise ratio (SINR) maximization problem is formulated by jointly optimizing ground base station's beam components and IRS's phase shift matrix. To address this challenging problem, we decouple the optimization problem into two subproblems, which are then solved by leveraging semi-definite relaxation, the bisection method, and eigenvalue decomposition techniques. Finally, the adaptive dual beams are generated by linearly weighting the obtained beam components, each of which is well-matched to the corresponding moving UAV. Numerical results reveal that the proposed beam tracking scheme not only enhances the worst-case UAV's performance but also guarantees a sufficient SINR demanded across the entire HSMUAVN.

Keywords: UAVs communication network; IRS; max-min optimization problem; beam tracking

check for updates

Academic Editor: Sergio Toral Marín

Received: 3 October 2025
Revised: 25 October 2025
Accepted: 30 October 2025
Published: 5 November 2025

Citation: Peng, Z.; Huang, G.; Deng, Q.; Liang, X. Adaptive Dual-Beam Tracking for IRS-Assisted High-Speed Multi-UAV Communication Networks. *Sensors* **2025**, *25*, 6757. https://doi.org/10.3390/s25216757

Copyright: © 2025 by the authors. Licensee MDPI, Basel, Switzerland. This article is an open access article distributed under the terms and conditions of the Creative Commons Attribution (CC BY) license (https://creativecommons.org/licenses/by/4.0/).

1. Introduction

Unmanned aerial vehicles (UAVs) play a paramount role in wireless communication networks due to their low cost, high maneuverability, and on-demand deployment capabilities [1–4]. However, providing stable and reliable communications for multiple high-speed UAVs remains a significant challenge. Especially for edge UAVs, the instability of beam gain is more pronounced due to severe channel fading and rapid changes [5]. Existing beam tracking schemes are fragile in highly dynamic environments, and the acquired channel state information (CSI) becomes obsolete almost instantaneously. Therefore, it is imperative to investigate the beam tracking schemes that dynamically adapt to high mobile UAVs to promptly establish stable links in high-speed multi-UAV networks (HSMUAVNs).

1.1. Related Works

Recently, UAVs have been seamlessly integrated into a broad spectrum of industries, spanning agriculture, survey mapping, vehicular communication, disaster response, and so on. Considering that task-driven UAVs operate at high velocities, maintaining accurate beam tracking presents substantial challenges in practical scenarios [6–9]. Firstly, the direct tracking of UAVs' direction-of-arrival (DoA) and direction-of-departure (DoD) incurs inherent latency due to UAV mobility and dynamic perturbations, resulting in beam misalignment and degraded link performance; secondly, employing beam training for CSI estimation leads to extensive feedback overhead, inherent estimation errors, and increased resource consumption; thirdly, existing narrow beam tracking methods face challenges in maintaining stable and robust beam gain. Intelligent reflecting surfaces (IRSs) possess the ability to dynamically reconfigure the wireless environment [10–12]. Therefore, integrating IRS into high-speed multi-UAV networks (HSMUAVNs) brings several notable advantages which include (1) compensating the high path loss and building blockages; (2) canceling interferences among UAVs; (3) steering the signal toward areas that are challenging to cover and improving worst-case UAV performance. However, scant attention has been paid to IRS-assisted beam tracking in high dynamic scenarios which generates high angular speeds. In [13], the roadside IRS and vehicle-side IRS beam tracking strategies were proposed in high-mobility vehicle communications, and a performance comparison between these two practice IRS deployment schemes was provided. However, these strategies were tailored to vehicular networks, whose channel variations are significantly slower than those induced by UAVs. Hence, they may prove vulnerable in HSMUAVNs, as the acquired CSI rapidly becomes obsolete. In [8], an integration of sensing and communications (ISAC)-assisted beam tracking scheme in multipath channels is proposed, but it came at the cost of beam training time. In [14], the geometry dynamic channel model and a deep learning-based channel narrow beam tracking method with small pilot overheads in IRS-assisted single UAV communication were proposed; however, this work overlooks beam misalignment inherent in highly dynamic UAV scenarios. As an alternative to the existing narrow beam tracking, angle-aware beam tracking schemes have been considered to reach beam alignment for UAV-GBS links. Ref. [15] pointed out that beam coverage is a key factor in beam reconstruction for high-speed UAV networks and proposed an efficient beam alignment framework integrating channel tracking and beamforming design, but it did not involve IRS and did not fully consider the severe channel fading and rapid channel changes for edge users in HSMUAVNs.

1.2. Motivations and Contributions

Unlike the existing works, we highlight how designing an adaptive dual-beam pattern based on the predicted spatial angle information (SAI) reduces the beam misalignment in HSMUAVN scenario. Moreover, the proposed adaptive dual-beam tracking simultaneously boosts the worst-case UAV's performance and maintains a reliable communication link across the entire HSMUAVN. The main contributions of this paper include the following:

(1) The attention-based double-layer long short-term memory (DL-LSTM) neural network is exploited to effectively predict the SAI of each high-speed UAV for the next frame. Therefore, the knowledge of each UAV's trajectory or angular transition model is not required. Then, the optimal beam coverage (BC) and the number of beam components for each UAV can be efficiently estimated based on the predicted SAI, which fully considered the prediction errors, the angular process noise, and the high-speed UAV motion, and always supports the coverage of high-speed UAVs within a frame.
(2) To enhance the edge UAV's performance and maintain a reliable communication link in HSMUAVNs, a worst-case UAV's received beam components signal-to-interference

plus noise ratio (SINR) maximization problem is formulated by jointly optimizing GBS's beam components and IRS's phase shift matrix (PSM). Furthermore, the formulated non-convex problem is effectively tackled by an iterative algorithm based on semi-definite relaxation, the bisection method, and eigenvalue decomposition techniques.

(3) Based on the acquired optimal BC and beam components, we design an adaptive dual-beam tracking scheme which is generated by linearly weighting these beam components. Simulation results validate that the proposed adaptive dual-beam tracking scheme improves both the achievable rate and robustness of the worst-case UAV in IRS-assisted HSMUAVNs.

1.3. Organization and Notations

In Section 2, we propose the IRS-assisted HSMUAVN system model. In Section 3, we design an adaptive dual-beam tracking algorithm and formulate the worst-case UAV's received beam components SINR maximization problem. Furthermore, we provide the complexity analysis. The simulation results and the conclusion are presented in Sections 4 and 5, respectively.

Notations: Lower-case, bold-face lower-case and bold-face capital letters represent scalars, vectors, and matrices, respectively. $\|\cdot\|$ signifies the Euclidean norm, while $|\cdot|$ represents the absolute value. Operation symbol $\otimes$ represents two vectors' element-wise multiplication. Finally, $\mathcal{CN}(\mu, \sigma^2)$ represents a random variable that follows the circularly symmetric complex Gaussian distribution with μ mean and σ^2 variance.

2. System Model

As shown in Figure 1, the considered IRS-assisted HSMUAVNs consist of K single-antenna moving UAVs, a building-mounted IRS equipped with $N_r = N_{rx} \times N_{rz}$ passive reflective elements, a GBS with $N = N_x \times N_z$ antennas, and $M = M_x \times M_z$ radio frequency chains. Moreover, a uniform planar array (UPA) is adopted at both the BS and the IRS [16,17]. Specifically, the GBS communicates with K high-speed UAVs with the aid of IRS. In the considered HSMUAVNs in Figure 1, the duration of the adaptive dual-beam tracking scheme includes a predicting slot (PS) and L_s tracking slots (TS). The PS mainly consists of an initial training data acquisition block, a channel estimation block, a beam alignment block, and a data transmission block, while the TS involves the current data feedback block, a beam alignment block, and a data transmission block. The initial training data acquisition block serves as a preparatory step prior to establishing reliable GBS-to-UAV links. Next, the channel estimation block adopts a deep learning-based method to accurately estimate the SAIs of each UAV node without invoking any beam sweeping procedure. Here, a time slot is denoted by Δt and the length of a beam tracking duration is denoted by $\Delta t * L_s$. As a matter of fact, because IRSs and UAVs are usually located at high altitudes, there exists of line-of-sight (LoS) paths between IRS-related and UAV-related channels. Thus, the GBS-IRS, GBS-UAVs, and IRS-UAVs links can be modeled as reasonable Rician fading channels [18]. Thus, the channel gain of the GBS-IRS link is given by

$$\mathbf{G} = \sqrt{\rho_{\mathrm{B-R}} d_{\mathrm{B-R}}^{-\Gamma_{\mathrm{B-R}}} \frac{\kappa_{\mathrm{B\text{-}R}}}{\kappa_{\mathrm{B\text{-}R}}+1}}\, \mathbf{a_R}(u_{\mathrm{B\text{-}Ra}}, v_{\mathrm{B\text{-}Ra}}) \mathbf{a_B}^T(u_{\mathrm{B\text{-}R}}, v_{\mathrm{B\text{-}R}}) + \sqrt{\rho_{\mathrm{B-R}} d_{\mathrm{B-R}}^{-\Gamma_{\mathrm{B-R}}} \frac{1}{\kappa_{\mathrm{B\text{-}R}}+1}} \tilde{\mathbf{H}}_{\mathrm{B\text{-}R}}, \quad (1)$$

where $\rho_{\mathrm{B-R}}$, $d_{\mathrm{B-R}}$, $\Gamma_{\mathrm{B-R}}$ and $\kappa_{\mathrm{B-R}}$ represent the reference path loss, the link distance, the path loss exponent, and the Rician factor, respectively. The relevant SAIs are denoted by $u_{\mathrm{B-R}} \triangleq \cos\theta_{\mathrm{B-R}} \cos\phi_{\mathrm{B-R}}$, $v_{\mathrm{B-R}} \triangleq \cos\theta_{\mathrm{B-R}}$, $u_{\mathrm{B-Ra}} \triangleq \cos\theta_{\mathrm{B-Ra}} \cos\phi_{\mathrm{B-Ra}}$, and $v_{\mathrm{B\text{-}Ra}} \triangleq \cos\theta_{\mathrm{B\text{-}Ra}}$. Since the established Rician fading channels are dominated by the LoS component,

accurately tracking the spatial angles of multi-UAVs is critical for CSI estimation. This will be discussed in Subsection III-A. Here, $\theta_{\mathrm{B-R}}$ and $\phi_{\mathrm{B-R}}$ represent the elevation and azimuth angles from GBS to IRS, respectively. Correspondingly, $\theta_{\mathrm{B-Ra}}$ and $\phi_{\mathrm{B-Ra}}$ represent the elevation and azimuth angles from IRS to GBS, respectively. $\tilde{\mathbf{H}}_{\mathrm{B-R}}$ represents the random non-line of sight (NLoS) component. The GBS's antennas and the IRS's reflective elements are located in the $x-z$ plane. It is assumed that the GBS is linked to the IRS controller via a feedback channel, enabling them to exchange information such as CSI, PSM, and so on. Then, the array responses of GBS and IRS are expressed as

$$\mathbf{a_B}(u,v) = \left[1,\ldots,e^{-j\pi\frac{2d_{GBS}}{\lambda}[(n_x-1)u+(n_z-1)v]}\right]^T, \tag{2}$$

$$\mathbf{a_R}(u,v) = \left[1,\ldots,e^{-j\pi\frac{2d_{IRS}}{\lambda}[(n_{rx}-1)u+(n_{rz}-1)v]}\right]^T, \tag{3}$$

where $n_x \in \{1,\cdots,N_x\}$, $n_z \in \{1,\cdots,N_z\}$, $n_{rx} \in \{1,\cdots,N_{rx}\}$ and $n_{rz} \in \{1,\cdots,N_{rz}\}$. d_{BS}, d_{IRS}, and λ denote the antenna spacing of GBS, the reflective element spacing of IRS, and the wavelength, respectively. Here, d_{GBS} and d_{IRS} is set as $d_{GBS} = d_{IRS} = \lambda/2$. Correspondingly, the IRS-UAV$_k$ and GBS-UAV$_k$ links are given by

$$\mathbf{h}_\alpha^H = \sqrt{\rho_\alpha d_\alpha^{-\Gamma_\alpha}\frac{\kappa_\alpha}{\kappa_\alpha+1}}\mathbf{a_R}^T(u_\alpha,v_\alpha) + \sqrt{\rho_\alpha d_\alpha^{-\Gamma_\alpha}\frac{1}{\kappa_\alpha+1}}\tilde{\mathbf{h}}_\alpha^H, \tag{4}$$

where ρ_α, d_α, Γ_α, and κ_α represent the reference path loss, the link distance, the path loss exponent, and the Rician factor, respectively. $\tilde{\mathbf{h}}_\alpha^H$ represents the NLoS component. $\alpha \in \{\mathrm{R-U}_k, \mathrm{B-U}_k\}$ represents the set of IRS-UAV$_k$ and GBS-UAV$_k$ links. Notably, the relevant SAI u_α and v_α are similar to the previous definition. In addition, advanced Doppler shift estimation and compensation techniques are employed to refine the estimation process and ensure robust compensation performance [19,20]. For simplicity, the Doppler shift induced by HSMUAVNs is assumed to be compensated. Moreover, because both the antenna and reflecting elements undergo the same Doppler shift, the SAIs are regarded as immune to the resulting frequency offset [15]. In this paper, we aim to devise an adaptive dual-beam pattern predicated upon the predicted SAI so as to mitigate beam misalignment, augment the performance of the worst-case UAV, and sustain the reliable communication links in HSMUAVNs. This work may be further extended by incorporating more practical IRS-HSMUAVN channel models that account for Doppler shifts, propagation delays, and other factors. The UAV$_k$'s received signal can be expressed as

$$y_k = \mathbf{h}_{\mathrm{B-U_k}}^H \sum_{k=1}^{K}\mathbf{w}^{(k)}s_k + \mathbf{h}_{\mathrm{R-U_k}}^H\mathbf{\Theta G}\sum_{k=1}^{K}\mathbf{w}^{(k)}s_k + u_k, \tag{5}$$

where u_k denotes the additive white Gaussian noise, $\sum_{k=1}^{K}\mathbf{w}^{(k)}s_k$ represents the signals sent by GBS. Here, $\mathbf{w}^{(k)} \in \mathbb{C}^{N\times 1}$ represents the corresponding beamforming vector from GBS to UAV$_k$, s_k represents the intended data for UAV$_k$, and $\mathbf{\Theta}$ represents IRS's PSM.

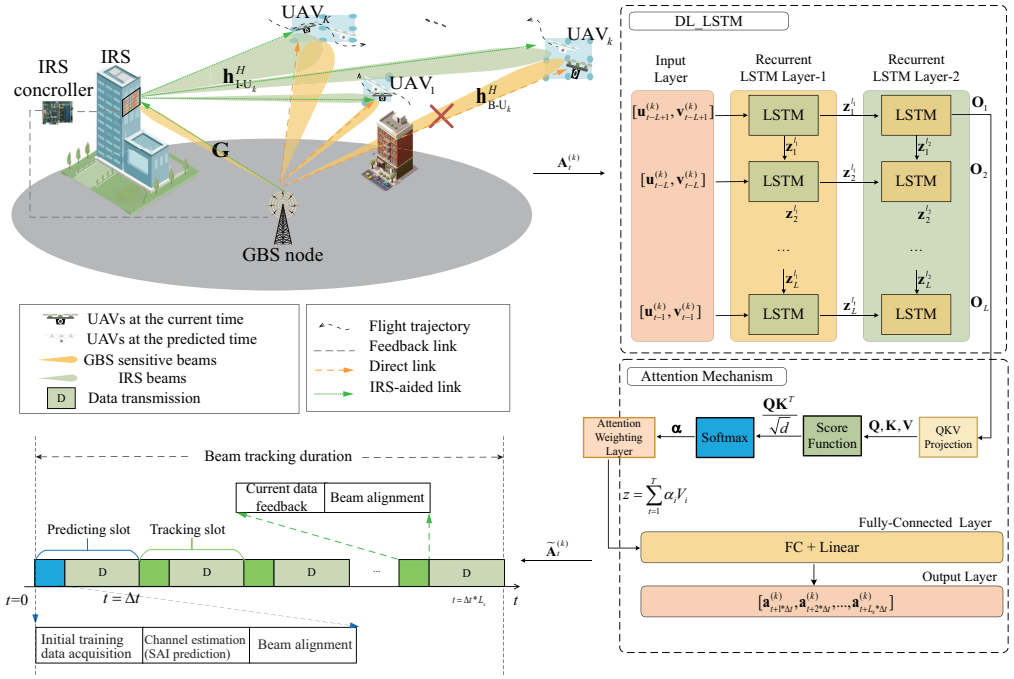


Figure 1. Adaptive dual-beam tracking scheme for IRS-assisted HSMUAVNs.

3. Adaptive Dual-Beam Tracking Algorithm Design and Optimization

3.1. UAVs' SAI Prediction Model

To fully exploit the temporal dynamics of UAVs, an attention-based double-layer LSTM (DL-LSTM) network [21,22] is employed to predict the multi-UAVs' SAIs in the PS phase, providing accurate estimates of the beam coverage bound and the required number of beam components. These estimates enable adaptive determination that efficiently avoids beam misalignment. The primary advantage of the attention-based DL-LSTM lies in its ability to construct sequence models that effectively observe the dynamic SAI of multi-UAV. It adeptly captures correlations and dependencies across various time steps, including those from the past, while minimizing the influence of irrelevant and redundant information [22,23]. Note that during the PS, the UAVs can leverage the low-frequency band to feed its current SAI back to the GBS [24]. As shown in Figure 1, the attention-based DL-LTSM-enabled spatial angle prediction model consists of an input layer, recurrent LSTM layer-1, recurrent LSTM layer-2, a fully connected (FC) layer, an output layer, and a attention mechanism. The hyperparameters of the proposed attention-based DL-LTSM-enabled SAI prediction model are shown in Figure 1. The specific description of the attention-based DL-LTSM-enabled SAI prediction model is as follows:

(1) The historical SAI sequence of UAVs are used as the input layer's data. For example, the past L-length SAI sequence of UAV$_k$ is denoted as

$$\mathbf{A}_t^{(k)} = [\mathbf{a}_{t-(L-1)*\Delta t}^{(k)}, \ldots, \mathbf{a}_{t-1*\Delta t}^{(k)}, \mathbf{a}_t^{(k)}] = \begin{bmatrix} u_{t-(L-1)*\Delta t}^{(k)}, \ldots, u_{t-1*\Delta t}^{(k)}, u_t^{(k)} \\ v_{t-(L-1)*\Delta t}^{(k)}, \ldots, v_{t-1*\Delta t}^{(k)}, v_t^{(k)}, \end{bmatrix} \tag{6}$$

where $\mathbf{a}_t^{(k)} = [u_t^{(k)}, v_t^{(k)}]^T$ denotes the SAI of UAV$_k$ at time slot t. This sequence is fed into a dual-layer LSTM network to extract temporal features. Then, the learned features of multi-UAVs' SAI in recurrent LSTM layer-2 is denoted as

$$\mathbf{O} = [\mathbf{o}_1, \mathbf{o}_2, \mathbf{o}_i, \ldots, \mathbf{o}_S]^{\mathrm{T}}, \tag{7}$$

where $\mathbf{o}_i$ represents the hidden feature vector at the i-th time step, and S denotes the sliding window size.

(2) The attention mechanism layer receives the learned features sequence $\mathbf{O}$ and maps it into query ($\mathbf{Q}$), key ($\mathbf{K}$), and value ($\mathbf{V}$) matrices via learnable weights, which are expressed as

$$\mathbf{Q} = \mathbf{W}_q\mathbf{O} + \mathbf{B}_q, \tag{8}$$

$$\mathbf{K} = \mathbf{W}_k\mathbf{O} + \mathbf{B}_k, \tag{9}$$

$$\mathbf{V} = \mathbf{W}_v\mathbf{O} + \mathbf{B}_v, \tag{10}$$

where $\mathbf{W}_q, \mathbf{W}_k, \mathbf{W}_v$ and $\mathbf{B}_q, \mathbf{B}_k, \mathbf{B}_v$ represent the trainable parameters.

(3) Then, the corresponding attention scores, which reflect the significance of the learned features, are computed using the scaled dot-product as

$$\text{Scores} = \frac{\mathbf{Q}\mathbf{K}^T}{\sqrt{d}}, \tag{11}$$

where d denotes the feature dimension. Next, applying softmax yields the attention weights as

$$\boldsymbol{\alpha} = \text{softmax}\left(\frac{\mathbf{Q}\mathbf{K}^T}{\sqrt{d}}\right), \tag{12}$$

where $\boldsymbol{\alpha} = [\alpha_1, \alpha_2, \ldots \alpha_S]$ denotes the attention vector. In the following, these weighted features linked to the attention weighting layer are calculated by

$$\mathbf{Z} = \boldsymbol{\alpha} \otimes \mathbf{V} = \sum_{i=1}^{T} \alpha_i v_i, \tag{13}$$

Here, $\mathbf{V} = [v_1, v_2, \cdots, v_S]^T$.

(4) The weighted feature $\mathbf{Z}$ is passed to the FC layer and activation function for further processing. Then, the output of the attention-based DL-LSTM SAI prediction model is given by

$$\widetilde{\mathbf{A}}_t^{(k)} = [\mathbf{a}_{t+1*\Delta t}^{(k)}, \mathbf{a}_{t+2*\Delta t}^{(k)}, \ldots, \mathbf{a}_{t+L_s*\Delta t}^{(k)}] = \begin{bmatrix} u_{t+1*\Delta t}^{(k)}, u_{t+2*\Delta t}^{(k)}, \ldots, u_{t+L_s*\Delta t}^{(k)} \\ v_{t+1*\Delta t}^{(k)}, v_{t+2*\Delta t}^{(k)}, \ldots, v_{t+L_s*\Delta t}^{(k)} \end{bmatrix}. \tag{14}$$

Here, $\mathbf{a}_{t+L_s*\Delta t}^{(k)} = g_\varsigma(\mathbf{M} f_\lambda(\mathbf{A}_t^{(k)}) + \mathbf{b})$, where $g_\varsigma(\cdot)$, $\mathbf{b}$, and $\mathbf{M}$ represent the nonlinear activation function, the weights, and the bias of the FC layer, respectively. Additionally, for the sake of simplicity, $\mathbf{a}_{t+L_s*\Delta t}^{(k)}$ can be expressed as

$$\widetilde{\mathbf{A}}_t^{(k)} = g_\varsigma(\mathbf{M} f_\lambda(\mathbf{A}_t^{(k)}) + \mathbf{b}) = h_\phi(\mathbf{A}_t^{(k)}), \tag{15}$$

where $h_\phi(\mathbf{A}_t^{(k)})$ represents the general expression of the attention-based DL-LTSM SAI prediction model that contains the parameter $\phi = \{\lambda, \varsigma, \mathbf{M}, \mathbf{b}\}$. Moreover, during the model training process, we exploit the mean squared error (MSE) cost function to measure the difference between the predicted DL-LSTM spatial angle data and the true data, which is given by

$$G_{MSE}(\phi) = (1/2N) \sum_{n=1}^{N} ||\widehat{\mathbf{A}}_t^{(k),n} - h_\phi(\mathbf{A}_t^{(k),n})||^2, n \in \{1, 2, \cdots, N\}, \tag{16}$$

where $\widehat{\mathbf{A}}_t^{(k)} = [\mathbf{a}_{t+1*\Delta t}^{(k)}, \mathbf{a}_{t+2*\Delta t}^{(k)}, \ldots, \mathbf{a}_{t+L_s*\Delta t}^{(k)}]$. Here, $\widehat{\mathbf{A}}_t^{(k)}$ and $\mathbf{A}_t^{(k),n}$ denote the label and the input of the n-th training example, respectively. Finally, the output layer produced the predicted SAI. The parameter settings of the attention-based DL-LTSM-enabled SAI prediction model are given in Table 1.

Table 1. The attention-based DL-LTSM-enabled SAI prediction model.

Hyperparameter Name	Numerical Value
Input size of $\mathbf{A}_t^k$	$2 \times L$
Size of $z_i^{l_1}$ in LSTM layer-1	64×1
Size of $z_i^{l_2}$ in LSTM layer-2	64×1
Attention layer size of Query/Key/Value	64×64
FC layer activation function	Linear
Dropout Rate	0.2
Learning Rate	0.001
Epochs	500
Batch size	128
Output size of $\mathbf{a}_{t+\Delta_t}^k$	$2 \times T_s$

3.2. Estimation of Beam Coverage Area and Number of Beams per UAV

According to the 3σ criterion [15] and the predicted SAI, the width and length of the adaptive BC area for UAV_k can be calculated by

$$l_{u,t}^{(k)} = \left| u_t^{(k)} - \tilde{u}_t^{(k)} \right| + 3\left(\sigma_{tg,u}^{(k)} + \sigma_{tp,u}^{(k)} + \sigma_{tm,u}^{(k)} \right), \tag{17}$$

$$l_{v,t}^{(k)} = \left| v_t^{(k)} - \tilde{v}_t^{(k)} \right| + 3\left(\sigma_{tg,v}^{(k)} + \sigma_{tp,v}^{(k)} + \sigma_{tm,v}^{(k)} \right), \tag{18}$$

where $\sigma_{tg,u}^{(k)}(\sigma_{tg,v}^{(k)})$, $\sigma_{tp,u}^{(k)}(\sigma_{tp,v}^{(k)})$, and $\sigma_{tm,u}^{(k)}(\sigma_{tm,v}^{(k)})$ represent the standard deviation of the predicted SAI [15], the standard deviation of the process noise, and the measurement standard deviation at UAV_k, respectively. $\tilde{u}_t^{(k)}$ and $\tilde{v}_t^{(k)}$ denote the attention-based DL-LTSM predicted SAI in the next time slot, respectively.

In the following, the center of the BC area is denoted by $(u_{c,t}^{(k)}, v_{c,t}^{(k)})$, obtained via $u_{c,t}^{(k)} = \left(u_t^{(k)} + \tilde{u}_t^{(k)} \right)/2, v_{c,t}^{(k)} = \left(v_t^{(k)} + \tilde{v}_t^{(k)} \right)/2$. To compute the number of beams per UAV tailored to its motion, the length and width of the BC area are divided into K_x and K_z quantized values, respectively, where $K_x = \max(N_x, N_{rx})$, $K_z = \max(N_z, N_{rz})$. Thus, the quantized spatial angle on the u-axes and v-axes are expressed as $u_n^{(k)} = -1 + (2n - 1)/K_x,\ n = 1, 2, 3, \ldots, K_x$ and $v_n^{(k)} = -1 + (2n-1)/K_z,\ n = 1, 2, 3, \ldots, K_z$, respectively. Here, the quantized angle interval are $2/K_x$ and $2/K_z$. $\mathbf{\Lambda}[u_t^{(k)}]$ represents the quantized spatial angle in the $u_n^{(k)}$ that is closest to the $u_t^{(k)}$. Subsequently, the quantified center position of the BC area during a frame are expressed as $u_{\mathbf{\Lambda}}^{(k)} = \mathbf{\Lambda}[(u_t^{(k)} + \tilde{u}_t^{(k)})/2]$ and $v_{\mathbf{\Lambda}}^{(k)} = \mathbf{\Lambda}[(v_t^{(k)} + \tilde{v}_t^{(k)})/2]$, respectively, and the quantified BC area from GBS to UAV_k is expressed as

$$C_t^{(k)} = \left[\left(u_t^{(k)^-}, u_t^{(k)^+} \right), \left(v_t^{(k)^-}, v_t^{(k)^+} \right) \right], \tag{19}$$

where $u_t^{(k)^-}(v_t^{(k)^-})$ and $u_t^{(k)^+}(v_t^{(k)^+})$ denote the lower and upper bounds of the quantized BC on the $u(v)$-axes, which are given by $u_t^{(k)-} = \mathbf{\Lambda}[u_{\mathbf{\Lambda}}^{(k)} - l_{u,t}^{(k)}/2]$, $u_t^{(k)+} = \mathbf{\Lambda}[u_{\mathbf{\Lambda}}^{(k)} + l_{u,t}^{(k)}/2]$, $v_t^{(k)+} = \mathbf{\Lambda}[v_{\mathbf{\Lambda}}^{(k)} + l_{v,t}^{(k)}/2]$ and $v_t^{(k)-} = \mathbf{\Lambda}[v_{\mathbf{\Lambda}}^{(k)} - l_{v,t}^{(k)}/2]$, respectively. Then, the corresponding number of beam components is $M_t^{(k)} = M_{u,t}^{(k)} \times M_{v,t}^{(k)}$, where $M_{u,t}^{(k)}$ and $M_{v,t}^{(k)}$ denote the number of quantized points in $\left(u_t^{(k)^-}, u_t^{(k)^+} \right)$ and $\left(v_t^{(k)^-}, v_t^{(k)^+} \right)$, respectively. These values

can be calculated by $M_{u,t}^{(k)} = \mathbf{H}[u_t^{(k)+}] - \mathbf{H}[u_t^{(k)-}] + 1$ and $M_{v,t}^{(k)} = \mathbf{H}[v_t^{(k)+}] - \mathbf{H}[v_t^{(k)-}] + 1$, respectively. Here, $\mathbf{H}[\cdot]$ represents the round operation. Thus, $M_t^{(k)}$ beam components $(\mathbf{w}_1^{(k)}, \cdots, \mathbf{w}_{m_t}^{(k)}, \cdots, \mathbf{w}_{M_t^{(k)}}^{(k)})$ individually point towards each quantized point in the corresponding BC area $C_t^{(k)}$.

By linearly combining the GBS beam components, the transmit beams directed at UAV$_k$ and dynamically adapted to its BC boundary are expressed as

$$\mathbf{w}_t^{(k)} = (1/\sqrt{M_t^{(k)}}) \sum_{m_t=1}^{M_t^{(k)}} \mathbf{w}_{m_t}^{(k)} e^{jm_t\beta_k}, \tag{20}$$

where β_k denotes the beamforming parameter that achieves the minimum main lobe variance. Here, the optimal β_k can be obtained by utilizing the exhaustive search method. Furthermore, by exploiting 2π-periodic and even function of β_k, the search space is drastically reduced [25]. Thus, the transmit beamforming matrix of the GBS covering K high-speed moving UAVs can be expressed as

$$\mathbf{W}_t = [\mathbf{w}_t^{(1)}, \mathbf{w}_t^{(2)}, \ldots, \mathbf{w}_t^{(k)}, \ldots, \mathbf{w}_t^{(K)}]. \tag{21}$$

For the sake of simplicity, we utilize a passive IRS, which offers a clearer and more intuitive perspective. Here, IRS's PSM is denoted by $\mathbf{\Theta}_t = \mathrm{diag}(\xi_t)$, where $\xi_t = [e^{j\vartheta_1}, \ldots, e^{j\vartheta_{nr}}, \ldots, e^{j\vartheta_{Nr}}]^T$.

3.3. Optimization Problem

Maintaining stable channel conditions (e.g., SINR) throughout a frame is essential to prevent disconnection and packet loss. However, sustaining a high SINR becomes extremely challenging in HSMUAVNs, especially for edge UAVs. To provide fair, stable, and reliable communications for HSMUAVNs, the worst-case UAV's received beam components SINR maximization problem is formulated by jointly designing $\mathbf{w}_{m_t}^{(k)}$ and ξ_t, which is expressed as

$$\max_{\{\mathbf{w}_{m_t}^{(k)}, \xi_t\}} \quad \min(\gamma_1^{(k)}, \ldots, \gamma_{m_t}^{(k)}, \ldots, \gamma_{M_t^{(k)}}^{(k)}) \tag{22a}$$

$$\text{s.t.} \sum_{k=1}^{K} \sum_{m_t=1}^{M_t^{(k)}} \left\| \mathbf{w}_{m_t}^{(k)} \right\|^2 \le P_{GBS}, \tag{22b}$$

$$0 \le \vartheta_{n_r} \le 2\pi, n_r \in \{1, \ldots, N_r\}. \tag{22c}$$

where P_{GBS} denotes GBS's transmit power. Then, the received beam components SINR of UAV$_k$ is given by

$$\gamma_{m_t}^{(k)} = \frac{\left| (\mathbf{h}_{\mathrm{B}-m_t}^{(k)H} + \mathbf{h}_{\mathrm{R}-m_t}^{(k)H} \mathbf{\Theta}_t \mathbf{G}) \mathbf{w}_{m_t}^{(k)} \right|^2}{\sum_{k=1}^{K} \sum_{i=1, i\neq m_t}^{M_t^{(k)}} \left| \left(\mathbf{h}_{\mathrm{B}-m_t}^{(k)H} + \mathbf{h}_{\mathrm{R}-m_t}^{(k)H} \mathbf{\Theta}_t \mathbf{G} \right) \mathbf{w}_i^{(k)} \right|^2 + u_{m_t}^{(k)}}. \tag{23}$$

Owing to the strong coupling among variables, problem (22) is non-convex and intractable to solve directly. Therefore, we decouple it into two subproblems (i.e., the GBS's beam components optimization subproblem and the IRS's PSM optimization subproblem), and propose a joint optimization algorithm to solve these subproblems iteratively.

3.4. GBS's Beam Components Optimization

Given $\mathbf{\Theta}_t$, the GBS's beam components optimization subproblem $\mathcal{OP}1$ is given by

$$\mathcal{OP}1: \max_{\{\mathbf{w}_{m_t}^{(k)}, a\}} \quad a \tag{24a}$$

$$\text{s.t.} \quad \frac{\left|\tilde{\mathbf{h}}_{m_t}^{(k)} \mathbf{w}_{m_t}^{(k)}\right|^2}{\sum_{k=1}^{K} \sum_{i=1, i \neq m_t}^{M_t^{(k)}} \left|\tilde{\mathbf{h}}_{m_t}^{(k)} \mathbf{w}_i^{(k)}\right|^2 + u_{m_t}^{(k)}} \geq a, \tag{24b}$$

$$\sum_{k=1}^{K} \sum_{m_t=1}^{M_t^{(k)}} \left\|\mathbf{w}_{m_t}^{(k)}\right\|^2 \leq P_{GBS}, \tag{24c}$$

where $\tilde{\mathbf{h}}_{m_t}^{(k)} = \mathbf{h}_{\text{B-}m_t}^{(k)H} + \mathbf{h}_{\text{R-}m_t}^{(k)H} \mathbf{\Theta}_t \mathbf{G}$. Let $\mathbf{A}_{m_t}^{(k)} = \tilde{\mathbf{h}}_{m_t}^{(k)H} \tilde{\mathbf{h}}_{m_t}^{(k)}$, $\mathbf{B}_{m_t}^{(k)} = \mathbf{w}_{m_t}^{(k)} \mathbf{w}_{m_t}^{(k)H}$, and $\mathbf{\Omega}_{m_t}^{(k)} = \{\mathbf{B}_1^{(k)}, \cdots, \mathbf{B}_{m_t}^{(k)}, \cdots, \mathbf{B}_{M_t^{(k)}}^{(k)}\}$. Since $\left|\tilde{\mathbf{h}}_{m_t}^{(k)} \mathbf{w}_{m_t}^{(k)}\right|^2 = \text{Tr}(\mathbf{A}_{m_t}^{(k)} \mathbf{B}_{m_t}^{(k)})$, constraints (24b) and (24c) can be, respectively, rewritten as

$$rank(\mathbf{B}_{m_t}^{(k)}) \leq 1, \tag{25a}$$

$$a \leq \frac{\text{Tr}(\mathbf{A}_{m_t}^{(k)} \mathbf{B}_{m_t}^{(k)})}{\sum_{k=1}^{K} \sum_{i=1, i \neq m_t}^{M_t^{(k)}} \text{Tr}(\mathbf{A}_{m_t}^{(k)} \mathbf{B}_i^{(k)}) + u_{m_t}^{(k)}}, \tag{25b}$$

$$\sum_{k=1}^{K} \sum_{m_t=1}^{M_t^{(k)}} \text{Tr}(\mathbf{B}_{m_t}^{(k)}) \leq P_{GBS}. \tag{25c}$$

To satisfy $\mathbf{B}_{m_t}^{(k)} = \mathbf{w}_{m_t}^{(k)} \mathbf{w}_{m_t}^{(k)H}$, constraint (25a) needs to be added. However, it makes the subproblem $\mathcal{OP}1$ even trickier. For this reason, constraint (25a) needs to be relaxed by using semi-definite relaxation (SDR) [18]. Additionally, for the constraint (25b), since its right side contains fractional form, it is still a non-convex constraint. Thereby, constraint (25b) needs to be transformed to an equivalent form as follows:

$$a\left(\sum_{k=1}^{K} \sum_{i=1, i \neq m_t}^{M_t^{(k)}} \text{Tr}(\mathbf{A}_{m_t}^{(k)} \mathbf{B}_i^{(k)}) + u_{m_t}^{(k)}\right) - \text{Tr}(\mathbf{A}_{m_t}^{(k)} \mathbf{B}_{m_t}^{(k)}) \leq 0. \tag{26}$$

Thus, $\mathcal{OP}1$ can be rewritten as

$$\max_{\{\mathbf{B}_{m_t}^{(k)}, a\}} \quad a \tag{27a}$$

$$\text{s.t. } (25b), (25c). \tag{27b}$$

Accordingly, problem (27a) is quasi-convex, which can be solved by the bisection method. Finally, $\mathbf{w}_{m_t}^{(k)}$ can be found by applying the singular value decomposition (SVD) with the Gaussian randomization [26]. Specifically, by introducing a random vector $\mathbf{z}_1 \in \mathcal{CN}(0,1)$, the rank-one candidate solution can be written as $\tilde{\mathbf{w}}_{m_t}^{(k)} = \mathbf{U}\sqrt{\sum}\mathbf{z}_1 / \|\mathbf{z}_1\|$, where $\mathbf{U}$ and $\sum$ can be obtained by using the singular value decomposition (SVD), i.e.,$\mathbf{B}_{m_t}^{(k)} = \mathbf{U} \sum \mathbf{V}^H$. The randomized solution is tested with (27b) for the feasibility until the objective value of (27a) converges.

3.5. IRS's PSM Optimization

Given $\mathbf{w}_{m_t}^{(k)}$, $\mathbf{D}_{m_t}^{(k)H} = \mathbf{h}_{\text{B-}m_t}^{(k)H} + \mathbf{h}_{\text{R-}m_t}^{(k)H}\boldsymbol{\Theta}_t\mathbf{G} = \tilde{\xi}_t^H\mathbf{C}_{m_t}^{(k)}$, where $\tilde{\xi}_t = [\xi_t^T, 1]^H$, $\mathbf{C}_{m_t}^{(k)} = [diag(\mathbf{h}_{\text{R-}m_t}^{(k)H})\mathbf{G}; \mathbf{h}_{\text{B-}m_t}^{(k)H}]$. Thus, $\mathcal{OP}2$ can be written as

$$\mathcal{OP}2: \max_{\{\boldsymbol{\Theta}_t, a\}} \ a \tag{28a}$$

$$\text{s.t. } 0 \le \vartheta_{n_r} \le 2\pi, n_r = 1, \ldots, N_r, \tag{28b}$$

$$\frac{\left|\mathbf{D}_{m_t}^{(k)H}\mathbf{w}_{m_t}^{(k)}\right|^2}{\sum_{k=1}^{K}\sum_{i=1, i\neq m_t}^{M_t^{(k)}}\left|\mathbf{D}_{m_t}^{(k)H}\mathbf{w}_i^{(k)}\right|^2 + u_{m_t}^{(k)}} \ge a. \tag{28c}$$

Let $\mathbf{e}_{m_t m_t}^{(k)} = \mathbf{C}_{m_t}^{(k)}\mathbf{w}_{m_t}^{(k)}$, $\mathbf{E}_{m_t m_t}^{(k)} = \mathbf{e}_{m_t m_t}^{(k)}\mathbf{e}_{m_t m_t}^{(k)H}$; constraint (28c) can be transformed into

$$\frac{\text{Tr}(\mathbf{E}_{m_t m_t}^{(k)}\tilde{\zeta}_t)}{\sum_{k=1}^{K}\sum_{i=1, i\neq m_t}^{M_t^{(k)}}\text{Tr}(\mathbf{E}_{m_t i}^{(k)}\tilde{\zeta}_t) + u_{m_t}^{(k)}} \ge a, \tag{29}$$

where $\tilde{\zeta}_t = \tilde{\xi}_t\tilde{\xi}_t^H$. Constraint (29) is then transformed into

$$a\mathbf{E}_{\tilde{\zeta}}^{(k)} - \text{Tr}(\mathbf{E}_{m_t m_t}^{(k)}\tilde{\zeta}_t) \le 0, \tag{30}$$

where

$$\mathbf{E}_{\tilde{\zeta}}^{(k)} = \sum_{k=1}^{K}\sum_{i=1, i\neq m_t}^{M_t^{(k)}}\text{Tr}(\mathbf{E}_{m_t i}^{(k)}\tilde{\zeta}_t) + u_{m_t}^{(k)}, \tag{31}$$

and $\tilde{\zeta}_{t0}$ represents the feasible value of $\tilde{\zeta}_t$. Thereby, we can rewrite $\mathcal{OP}2$ as

$$\max_{\{\tilde{\zeta}_t, a\}} \ a. \tag{32a}$$

$$\text{s.t. (12), (14).} \tag{32b}$$

Problem (32) is quasi-convex, and thus, it can be efficiently solved via the bisection method. Additionally, EVD is adopted to obtain ξ_t based on $\tilde{\zeta}_t$.

Algorithm 1 summarizes the overall procedure. Furthermore, Figure 2 depicts a detailed flowchart of the UAV-specific SAI prediction and the iterative optimization process.

3.6. Complexity Analysis

Next, we analyze the complexity of the proposed joint optimization algorithm for the considered IRS-HSMUAVNs. The overall complexity comprises two primary parts. Specifically, since subproblem $\mathcal{OP}1$ is solved by the bisection method and the EVD, its complexity is $\mathcal{O}\left(log(a/\varepsilon_{op1}) + (N+1)^3\right)$. Similarly, the subproblem $\mathcal{OP}2$ is a non-convex problem which adopts the same solving method as $\mathcal{OP}1$, so the complexity used for computing IRS's PSM is $\mathcal{O}\left(log(a/\varepsilon_{op2}) + (N_r+2)^3\right)$. Thus, the overall complexity of the proposed joint optimization algorithm is

$$\mathcal{O}\left(Iter(log(a/\varepsilon_{op1}) + log(a/\varepsilon_{op2}) + (N+1)^3 + (N_r+2)^3)\right), \tag{33}$$

where $Iter$ denotes the required iteration numbers, ε_{op1} and ε_{op2} denote tolerance level. Note that the complexity of linearly weighting the obtained beam components is very low, almost negligible. Figure 4 demonstrates that the proposed algorithm achieves rapid convergence.

Algorithm 1 Adaptive dual-beam tracking algorithm

Require: $u_t^{(k)}$, $v_t^{(k)}$, $\tilde{u}_t^{(k)}$, $\tilde{v}_t^{(k)}$, β_k, $\mathbf{G}$, $\mathbf{h}_{\mathrm{R-U_k}}^H$, $\mathbf{h}_{\mathrm{B-U_k}}^H$, P_{GBS};

Initialize: ξ_{t0};
Based on $u_t^{(k)}$, $v_t^{(k)}$, $\tilde{u}_t^{(k)}$, $\tilde{v}_t^{(k)}$, calculate $l_{u,t}^{(k)}$, $l_{v,t}^{(k)}$, $M_t^{(k)}$;
repeat
  Given ξ_{t0}, update a and $\mathbf{B}_{m_t}^{(k)}$ by bisection method.
  repeat
    Given $a = a_{max}/2 \in [0, a_{max}]$, when $\mathbf{B}_{m_t}^{(k)}$ exists a feasible domain, the range of a has changed to $[a_{max}/2, a_{max}]$; Otherwise, the range of a is $[0, a_{max}/2]$.
    According to the range of a, the median value of a is calculated.
  until the range of a is small enough.
  Obtain $\mathbf{w}_{m_t}^{(k)}$ by applying EVD.
  Utilizing $\mathbf{w}_{m_t}^{(k)}$, update a and $\tilde{\xi}_t$ by bisection method.
  Obtain ξ_t by applying EVD.
  Update $\xi_{t0} \leftarrow \xi_t$.
until convergence
Calculate $\mathbf{W}_t = [\mathbf{w}_t^{(1)}, \mathbf{w}_t^{(2)}, \ldots, \mathbf{w}_t^{(k)}, \ldots, \mathbf{w}_t^{(K)}]$;

Ensure: $\mathbf{W}_t$,$\mathbf{\Theta}_t = \mathrm{diag}(\xi_t)$.

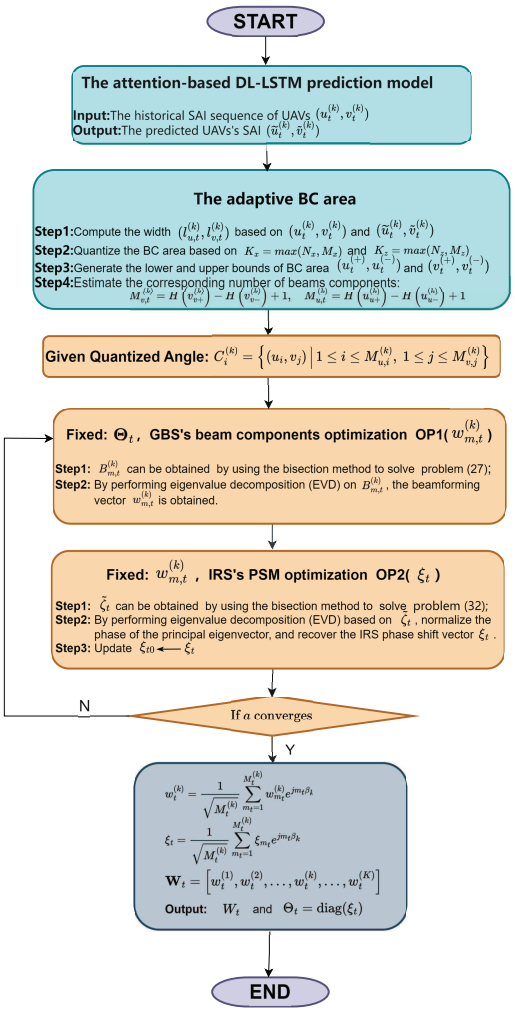


Figure 2. Flowchart of the adaptive dual-beam tracking algorithm.

4. Simulation Results

In this section, simulation results are provided to illustrate the performance of the proposed adaptive dual-beam tracking scheme for IRS-assisted HSMUAVNs. According to [15,27,28], the related simulation parameters are given as follows. For simulations, we consider that the speeds of UAVs are randomly determined in $\mathcal{U}$[170, 200][km/hr], where $\mathcal{U}$ represents uniform distribution. The number of UAVs K is set to 3. $\sigma_{tp,u} = \sigma_{tp,v} = 5 \cdot 10^{-3}$ and $\sigma_{tm,u} = \sigma_{tm,v} = 10^{-3}$. The initial location of each UAV is randomly generated in a space with a radius of 120 m around GBS. The location of GBS is given by (0 m, 0 m, 0 m). And the location of IRS is given by (0 m, −50 m, 50 m). Additionally, the Rician factor $\kappa_{\mathrm{B-I}} = \kappa_{\mathrm{I-U}_k} = 10\ dB$, $\kappa_{\mathrm{B-U}_k} = 5$ dB, and the path loss exponent $\chi_{\mathrm{B-I}} = \chi_{\mathrm{I-U}_k} = 2$ dB, $\chi_{\mathrm{B-U}_k} = 2.2$ dB. The time slot length $\Delta t = 20$ ms and $L_s = 3$. The neural network is retrained at every 60 ms.

Figure 3 shows the comparison between the actual spatial angles and the predicted spatial angles of high-speed multi-UAVs. Although the UAVs move at high speeds, it can be observed from Figure 3 that the spatial angle prediction error for each UAV remains consistently minimal at every moment. From Figure 3, the average displacement errors (ADE) between the actual and the predicted SAIs of UAV_1, UAV_2, and UAV_3 are 0.0147, 0.009, and 0.0143, respectively. Here, ADE denotes the average Euclidean distance between the actual and the predicted SAIs. Therefore, by utilizing the attention-based DL-LSTM, the GBS can effectively predict the spatial angles of high-speed multi-UAVs.

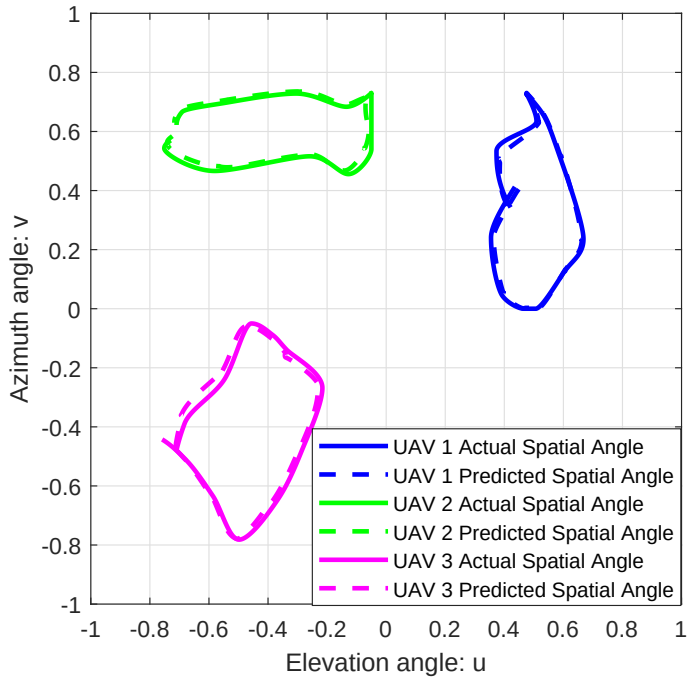


Figure 3. High-speed multi-UAVs trajectories in u-v plan.

Figure 4 depicts the proposed algorithm's convergence performance when $N = 64$, $N_r = \{81, 100, 121\}$ when $P_{GBS} = 30$ dB. It is shown that the worst-case UAV's received SINR can converge fast within five iterations. Furthermore, the worst-case UAV's received SINR performance enhances as N_R increases.

Figure 5 shows the worst-case UAV's achievable rate versus the transmitted SNR under different schemes. Here, "**Maximizing the sum-rate with IRS** " refers to UAVs' sum-rate maximization by jointly optimizing GBS's beamforming and IRS's PSM. "**Without IRS**" refers to the proposed beam tracking algorithm for GBS-UAV communications without the assistance of the IRS. As shown in Figure 5, compared with "**Maximizing the sum-**

rate with IRS", the proposed algorithm improves the achievable rate of the worst-case UAV by 170% when the transmitted SNR =30 dB, N = 64, and N_r = 169. This is because "**Maximizing the sum-rate with IRS**" benefits UAVs in good channel conditions but harms the worst-case UAV. Thus, such unfair resource allocation leads to a low achievable rate for the worst-case UAV. Additionally, the worst-case UAV's performance of "**Without IRS**" is obviously worse than that of the proposed algorithm. The major reason is that IRS offers more DoFs. Therefore, IRS's resources are beneficial for enhancing the communication capability of the worst-case UAV under the max–min fairness beam design scheme.

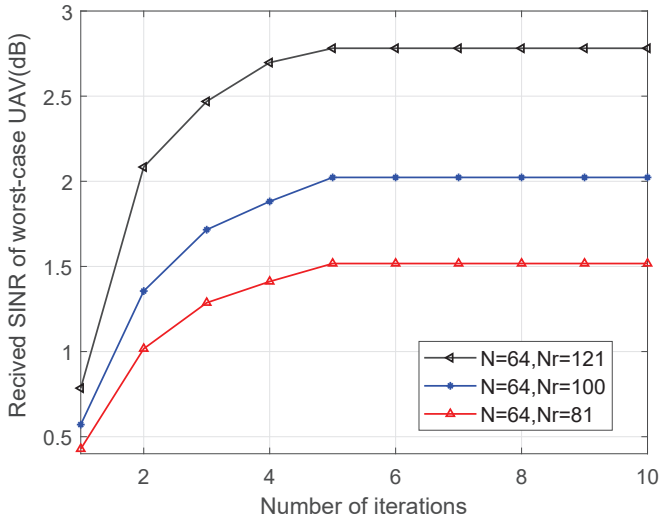


Figure 4. Received SINR of worst-case UAV versus number of iterations.

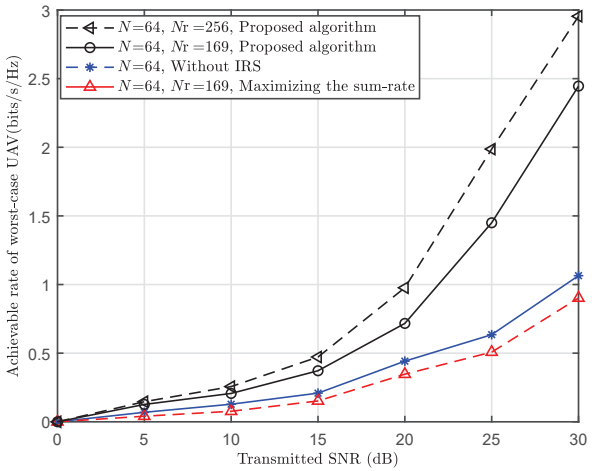


Figure 5. Achievable rate of worst-case UAV versus transmitted SNR (t = 35 ms).

Figures 6 and 7 depict the beamforming gain [dBm] of the existing beam tracking algorithm [15] and the proposed beam tracking algorithm, respectively. Here, the red boxes represent the BC areas corresponding to each moving UAV during a frame. As shown in Figure 6, the existing beam tracking algorithm suffers from limited coverage area when aligning with high-speed UAVs, failing to accommodate their full mobility range. This inherent limitation consequently leads to unstable communication performance and frequent link interruptions. In contrast, the proposed algorithm generates adaptive dual-beam coverage that maintains a precise tracking of each UAV's movement, as demonstrated in Figure 7, thereby ensuring stable and high-quality service for all mobile UAVs.

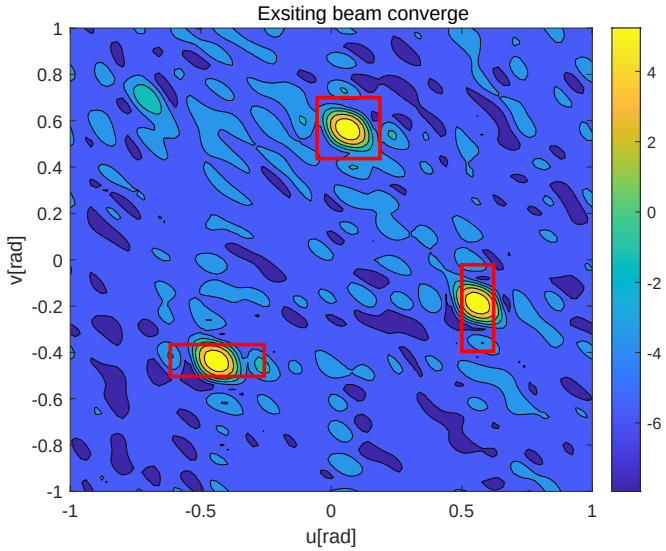


Figure 6. Exsiting beam converge of multi-UAVs.

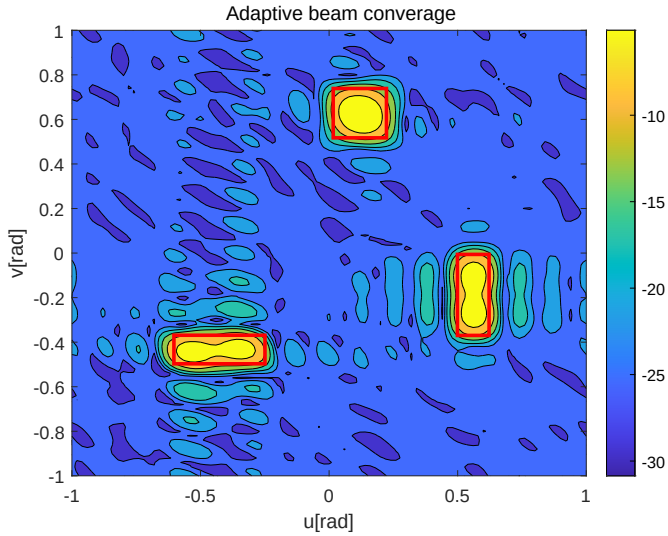


Figure 7. Adaptive beam converage of multi-UAVs.

Figure 8 further shows the worst-case UAV's beam gain, where the red boxes represent the BC area corresponding to each moving UAV, and the red dots represent the SAI of the worst-case UAV at the corresponding time $t = \{0, 20, 40, 60, 80, 100\}$ ms. From Figure 8, the existing algorithm only provides a good beam gain in the central point of the current and the next prediction moment of the worst-case UAV, but the beam gain decreases sharply in nearby areas. In contrast, the beam generated by the proposed algorithm always points to the potential moving area of the worst-case UAV.

To more intuitively show the beam tracking performance, the worst-case UAV's achievable rate versus time when $P_{GBS} = 30\ dB$ is presented in Figure 9. As shown in Figure 9, despite the help of IRS, "**Existing beam tracking**" outperforms the proposed algorithm at narrow beam alignment time, but its performance drops dramatically at other times, thereby easily resulting in link disconnection. At the same time, the performance of "**Maximizing the sum-rate with IRS**" also performs poorly and is instable compared with the other algorithms, since it benefits UAVs in favorable channels yet disadvantages those experiencing the worst-case CSI conditions. In contrast, the proposed algorithm always sustains the stable and robust performance of the worst-case UAV during a frame, since the worst-case UAV is given priority in the resources allocation under the min–max

optimization framework. Consequently, the proposed adaptive dual-beam tracking design achieves a well-balanced resource allocation, which is vital for ensuring fair, stable, and reliable communications in IRS-HSMUAVNs.

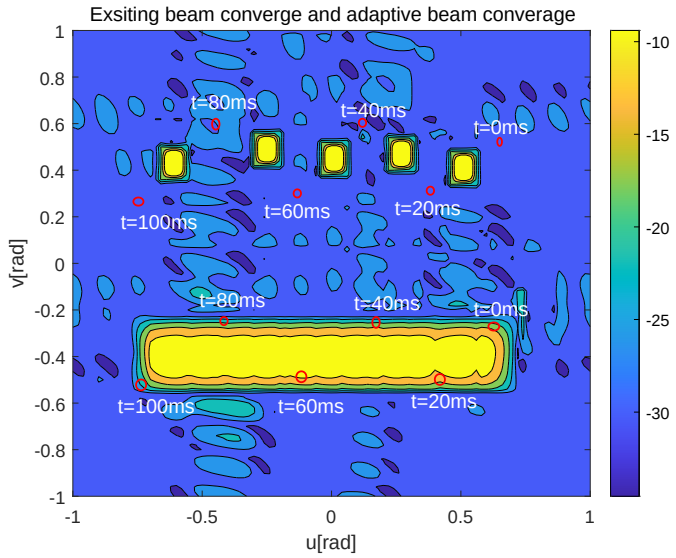


Figure 8. Contour map of beamforming gain of the exsiting beam tracking algorithm and the proposed adaptive beam tracking algorithm, when $N = 64$, $N_r = 64$, SNR = 10 dB.

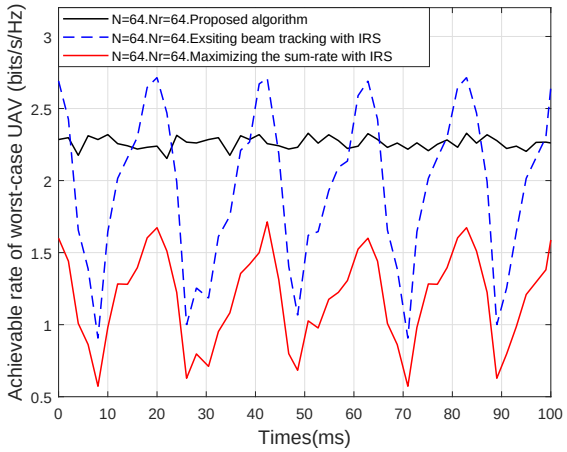


Figure 9. Achievable rate of worst-case UAV versus time.

5. Conclusions

In this paper, we studied a novel adaptive dual-beam tracking scheme in an adaptive mode for IRS-assisted HSMUAVNs. An attention-based DL-LSTM neural network was employed to estimate the BC and the beam components of the optimal beam direction for each high-speed UAV. Furthermore, we formulated a worst-case UAV's received beam components SINR maximization problem by jointly optimizing the beam components at the GBS and the PSM of IRS. To solve this optimization problem, we decouple it into two subproblems and iteratively addressed them using the semi-definite relaxation, bisection method, and eigenvalue decomposition techniques. Simulation results demonstrated that the proposed algorithm not only enhanced the worst-case UAV's performance but also maintained stable and robust communications throughout each frame. Furthermore, these results highlighted the critical importance of adaptive dual-beam tracking design in ensuring reliable communications across the entire HSMUAVNs. In future work, we will address the extension of channel tracking to a more realistic IRS-assisted HSMUAVN channel.

Author Contributions: Conceptualization, Z.P., G.H., Q.D. and X.L.; methodology, Z.P., G.H., Q.D. and X.L.; software, Z.P., G.H., Q.D. and X.L.; validation, Z.P., G.H., Q.D. and X.L.; formal analysis, Z.P., G.H., Q.D. and X.L.; investigation, Z.P., G.H., Q.D. and X.L.; resources, Z.P., G.H., Q.D. and X.L.; writing—original draft preparation, Z.P., G.H., Q.D. and X.L.; writing—review and editing, Z.P., G.H., Q.D. and X.L. All authors have read and agreed to the published version of the manuscript.

Funding: This work was supported in part by the National Natural Science Foundation of China under Grant 62261019, in part by Hainan Provincial Natural Science Foundation of China under Grant 625MS052, and in part by the Scientific Research Fund Project of Hainan University under Grant KYQD(ZR)-21132.

Institutional Review Board Statement: Not applicable.

Informed Consent Statement: Not applicable.

Data Availability Statement: No new data were created or analyzed in this study.

Conflicts of Interest: The authors declare no conflicts of interest.

References

1. Liang, X.; Zhang, Z.; Deng, Q.; Shu, F.; Liu, S.; Wang, J. Joint Trajectory and Primary-Secondary Transmission Design for UAV-Carried-IRS Assisted Underlay CR Networks. *IEEE Trans. Veh. Technol.* **2024**, *73*, 17848–17853. [CrossRef]
2. Mu, J.; Zhang, R.; Cui, Y.; Gao, N.; Jing, X. UAV Meets Integrated Sensing and Communication: Challenges and Future Directions. *IEEE Commun. Mag.* **2023**, *61*, 62–67. [CrossRef]
3. Gao, N.; Qin, Z.; Jing, X.; Ni, Q.; Jin, S. Anti-Intelligent UAV Jamming Strategy via Deep Q-Networks. *IEEE Trans. Commun.* **2020**, *68*, 569–581. [CrossRef]
4. Deng, Q.; Yu, G.; Liang, X.; Zhang, Z.; Shu, F.; Li, X.; Wang, J. Sensing-Transmission-Energy Trade-off for IRS-Assisted Cognitive UAV Communication Systems. *IEEE Trans. Cogn. Commun. Netw.* **2025**, 1–15. [CrossRef]
5. Deng, Q.; Chen, X.; Liang, X.; Shu, F.; Du, J. Adaptive Beam Alignment and Optimization for IRS-Aided High-Speed UAV Communications. *IEEE Trans. Green Commun. Netw.* **2023**, *7*, 1583–1595. [CrossRef]
6. Min, K.; Park, H.S.; Lee, H.S. Beam Alignment for Non-Stationary Enviroments Using a Novel Time-Varying Structured Bandit. *IEEE Trans. Veh. Technol.* **2025**, *74*, 6727–6732. [CrossRef]
7. Yang, L.; Zhang, W. Beam Tracking and Optimization for UAV Communications. *IEEE Trans. Wireless Commun.* **2019**, *18*, 5367–5379. [CrossRef]
8. Cui, Y.; Zhang, Q.; Feng, Z.; Wen, Q.; Liu, F.; Zhang, P. Seeing Is Not Always Believing: ISAC-Assisted Predictive Beam Tracking in Multipath Channels. *IEEE Wirel. Commun. Lett.* **2024**, *13*, 14–18. [CrossRef]
9. Wang, Y.; Tang, Z.; Huang, A.; Zhang, H.; Chang, L.; Pan, J. Placement of UAV-Mounted Edge Servers for Internet of Vehicles. *IEEE Trans. Veh. Technol.* **2024**, *73*, 10587–10601. [CrossRef]
10. Liang, X.; Huang, L.; Deng, Q.; Shu, F.; Yu, G.; Wang, J. IRS-Assisted Spectrum Sensing and Primary-Secondary Transmission for Cognitive Radio Networks. *IEEE Trans. Cogn. Commun. Netw.* **2025**, *11*, 1508–1521. [CrossRef]
11. Wang, C.; Li, Z.; Zheng, T.X.; Ng, D.W.K.; Al-Dhahir, N. Intelligent Reflecting Surface-Aided Full-Duplex Covert Communications: Information Freshness Optimization. *IEEE Trans. Wirel. Commun.* **2023**, *22*, 3246–3263. [CrossRef]
12. Wang, Z.; Wu, W.; Zhou, F.; Wang, B.; Wu, Q.; Quek, T.Q.S.; Chae, C.B. IRS-Enhanced spectrum sensing and secure transmission in cognitive radio networks. *IEEE Trans. Wirel. Commun.* **2024**, *23*, 10271–10286. [CrossRef]
13. Huang, Z.; Zhu, L.; Zhang, R. Intelligent Surfaces Aided High-Mobility Communications: Opportunities and Design Issues. *IEEE Commun. Mag.* **2024**, *62*, 122–128. [CrossRef]
14. Yu, J.; Liu, X.; Gao, Y.; Zhang, W. Deep Learning for Channel Tracking in IRS-Assisted UAV Communications Systems. *IEEE Trans. Wirel. Commun.* **2022**, *21*, 7711–7722. [CrossRef]
15. Song, H.L.; Ko, Y.C. Beam Alignment for High-Speed UAV via Angle Prediction and Adaptive Beam Coverag. *IEEE Trans. Veh. Technol.* **2021**, *70*, 10185–10192. [CrossRef]
16. Hu, X.; Zhong, C.; Zhang, Z. Angle-Domain Intelligent Reflecting Surface Systems: Design and Analysis. *IEEE Trans. Commun.* **2021**, *69*, 4202–4215. [CrossRef]
17. Mu, X.; Liu, Y.; Guo, L.; Lin, J.; Schober, R. Joint Deployment and Multiple Access Design for Intelligent Reflecting Surface Assisted Networks. *IEEE Trans. Wirel. Commun.* **2021**, *20*, 6648–6664. [CrossRef]
18. Deng, Q.; Yu, G.; Liang, X.; Shu, F.; Wang, J. Joint Trajectory, Sensing, and Transmission Design for IRS-Assisted Cognitive UAV Systems. *IEEE Wirel. Commun. Lett.* **2024**, *13*, 233–237. [CrossRef]

19. Zhang, Q.; Sun, H.; Feng, Z.; Gao, H.; Li, W. Data-Aided Doppler Frequency Shift Estimation and Compensation for UAVs. *IEEE Internet Things J.* **2020**, *7*, 400–415. [CrossRef]
20. Liang, X.; Deng, Q.; Shu, F.; Wang, J. Energy-Efficiency Joint Trajectory and Resource Allocation Optimization in Cognitive UAV Systems. *IEEE Internet Things J.* **2022**, *9*, 23058–23071. [CrossRef]
21. Liu, C.; Yuan, W.; Wei, Z.; Liu, X.; Ng, D.W.K. Location-Aware Predictive Beamforming for UAV Communications: A Deep Learning Approach. *IEEE Wirel. Commun. Lett.* **2021**, *10*, 668–672. [CrossRef]
22. Xing, X.; Wang, R.; Han, B.; Wu, C.; Xiao, B. A Trajectory Prediction Method of Drogue in Aerial Refueling Based on Transfer Learning and Attention Mechanism. *IEEE Trans. Instrum. Meas.* **2024**, *73*, 3531712–3531723. [CrossRef]
23. Chen, Z.; Wu, M.; Zhao, R.; Guretno, F.; Yan, R.; Li, X. Machine Remaining Useful Life Prediction via an Attention-based Deep Learning Approach. *IEEE Trans. Ind. Electron.* **2021**, *68*, 2521–2531. [CrossRef]
24. Ramasamy, D.; Venkateswaran, S.; Madhow, U. Compressive Tracking with 1000-element Arrays: A framework for Multi-Gbps mmWave Cellular Downlinks. In Proceedings of the 2012 50th Annual Allerton Conference on Communication, Control, and Computing (Allerton), Monticello, IL, USA, 1–5 October 2012; pp. 690–697.
25. Noh, S.; Zoltowski, M.D.; Love, D.J. Multi-Resolution Codebook and Adaptive Beamforming Sequence Design for Millimeter Wave Beam Alignment. *IEEE Trans. Wirel. Commun.* **2017**, *16*, 5689–5701. [CrossRef]
26. Yuan, J.; Liang, Y.C.; Joung, J.; Feng, G.; Larsson, E.G. Intelligent Reflecting Surface-Assisted Cognitive Radio System. *IEEE Trans. Commun.* **2021**, *69*, 675–687. [CrossRef]
27. Hu, X.; Zhong, C.; Zhang, Y.; Chen, X.; Zhang, Z. Location Information Aided Multiple Intelligent Reflecting Surface Systems. *IEEE Trans. Commun.* **2020**, *68*, 7948–7962. [CrossRef]
28. Li, S.; Duo, B.; Di Renzo, M.; Tao, M.; Yuan, X. Robust Secure UAV Communications with the Aid of Reconfigurable Intelligent Surfaces. *IEEE Trans. Wirel. Commun.* **2021**, *20*, 6402–6417. [CrossRef]

Disclaimer/Publisher's Note: The statements, opinions and data contained in all publications are solely those of the individual author(s) and contributor(s) and not of MDPI and/or the editor(s). MDPI and/or the editor(s) disclaim responsibility for any injury to people or property resulting from any ideas, methods, instructions or products referred to in the content.